# **Materials Advances**



View Article Online PAPER



Cite this: Mater. Adv., 2025, 6, 4874

Received 7th May 2025, Accepted 3rd June 2025

DOI: 10.1039/d5ma00454c

rsc.li/materials-advances

## Molecular interaction-induced thermoelectric performance enhancement of graphene thin films with an agglomerated conductive polymer†

Keito Uchida, ‡ a Shunya Sakane, 🕩 ‡ \* Takashi Shimizu, a Akito Ayukawa, b 

Graphene-based materials are anticipated to be used as thermoelectric conversion devices due to their flexibility and low toxicity, in addition to their high thermoelectric performance. In this study, we demonstrated an enhancement in the thermoelectric power factor of graphene thin films with agglomerated PEDOT:PSS through  $\pi-\pi$  interactions. The graphene/PEDOT:PSS thin films were prepared by a spin-coating method. Atomic force microscopy, X-ray diffraction and Raman spectroscopy revealed that PEDOT:PSS agglomerated on graphene thin films through  $\pi-\pi$  interactions. The fabricated sample exhibited a 1.6 times higher power factor compared to graphene single-phase thin films. The local  $\pi-\pi$ interactions with PEDOT:PSS contribute to the electron transfer from graphene to PEDOT and the enhanced crystallinity of graphene throughout the thin film, resulting in a high power factor. This study contributes to the development of graphene-based thermoelectric materials.

#### 1 Introduction

Thermoelectric materials are attracting attention as a clean energy source that directly converts thermal energy into electrical energy. The performance of thermoelectric materials is expressed by the dimensionless figure of merit ZT as shown below:

$$ZT = \frac{S^2 \sigma T}{\kappa},$$

where S,  $\sigma$ , T, and  $\kappa$  are the Seebeck coefficient (V K<sup>-1</sup>), electrical conductivity (S m<sup>-1</sup>), absolute temperature (K), and thermal conductivity (W m<sup>-1</sup> K<sup>-1</sup>), respectively. A high power factor  $S^2\sigma$  and a low  $\kappa$  are required to realize high thermoelectric performance. Conventional inorganic thermoelectric materials such as Sb<sub>2</sub>Te<sub>3</sub>, Bi<sub>2</sub>Te<sub>3</sub>, and PbTe and other compounds containing Te have shown high ZT. 1-3 Recently, Te-free compounds such as Mg<sub>3</sub>(SbBi)<sub>2</sub>, Cu<sub>2</sub>Se, and Ag<sub>2</sub>Se have shown

high thermoelectric performance comparable to that of the above Te-containing materials and are expected to become alternative materials. 4-13 Materials such as Si, Mg<sub>2</sub>Si, and FeSi<sub>2</sub>, which are composed of ubiquitous elemental materials, are also considered promising alternatives. 14-17

On the other hand, carbon-based materials such as diamond, carbon nanotubes, and graphene attract attention because they are composed of carbon, which is abundant in nature, and have excellent mechanical properties that make them widely applicable as wearable materials. 18-24 In particular, graphene, with its two-dimensional structure of carbon atoms arranged in a honeycomb lattice, has two fundamental unit vectors in reciprocal space with its unit cell. The two points at the corners of the Brillouin zone, corresponding to these unit vectors, are known as Dirac points. Near these Dirac points, graphene exhibits a unique electronic structure called the Dirac cone, 23,25-27 which contributes to its high mobility of 60 000 cm<sup>2</sup> V<sup>-1</sup> S<sup>-1</sup>.<sup>28</sup> In contrast, the Seebeck coefficient of graphene monolayers is extremely low because the Fermi level is located near Dirac points and both electrons and holes contribute to electrical conduction. 29,30 However, controlling the Fermi level by applying an electric field to the graphene monolayer allows for the selective control of the carrier conduction type and a consequent improvement of S. As a result, high  $S^2\sigma$ values of 360  $\mu$ W cm<sup>-1</sup> K<sup>-2</sup> (p-type) and 190  $\mu$ W cm<sup>-1</sup> K<sup>-2</sup> (n-type) have been reported for a micron-scale graphene monolayer.31-33 Graphene multilayers prepared by chemical vapor deposition (CVD) are capable of centimeter-scale thin film fabrication and have been

<sup>&</sup>lt;sup>a</sup> Faculty of Science and Engineering, Chuo University, 1-13-27, Kasuga, Bunkyo-ku, Tokyo, 112-8551, Japan. E-mail: htanaka@kc.chuo-u.ac.jp

<sup>&</sup>lt;sup>b</sup> Graduate School of Science and Engineering, Ibaraki University, 4-12-1, Nakanarusawa-cho, Hitachi, Ibaraki, 316-8511, Japan. E-mail: shunya.sakane.sz12@vc.ibaraki.ac.jp

<sup>†</sup> Electronic supplementary information (ESI) available: Cross-sectional SEM images of GP3, Raman spectra and AFM images of graphene and PEDOT:PSS single-phase thin films are included. In addition, the intensity of the 002 XRD patterns of GP<sub>n</sub> and G<sub>3</sub> samples is shown. See DOI: https://doi.org/10.1039/ d5ma00454c

<sup>‡</sup> These authors contributed equally to this work.

Paper

32.9  $\mu$ W cm<sup>-1</sup> K<sup>-2</sup> (n-type).<sup>34</sup>

reported to exhibit high  $S^2\sigma$  values of 69.3  $\mu$ W cm<sup>-1</sup> K<sup>-2</sup> (p-type) and

For practical applications, a high  $S^2\sigma$  is required without the application of an electric field. In a previous report, graphene thin films can be prepared through spin-coating using graphene ink, which has also demonstrated a relatively high S of 41  $\mu$ V K<sup>-1</sup> without the application of an electric field, resulting in an  $S^2\sigma$  of 0.187  $\mu W$  cm<sup>-1</sup> K<sup>-2</sup> (p-type).<sup>35</sup> To improve the thermoelectric properties of graphene thin films, compositing them with aromatic ring compounds such as poly(3,4ethylenedioxythiophene):poly(styrene sulfonate) (PEDOT:PSS) is effective because it improves crystallinity and enables electron transfer through  $\pi$ - $\pi$  interactions. In fact, the  $\pi$ - $\pi$  interaction has been demonstrated in various graphene composites such as rGO and graphene quantum dots (GQDs)/PEDOT:PSS. 36-42

In this study, graphene/PEDOT:PSS thin films were fabricated by a spin-coating method with the aim of obtaining high  $S^2\sigma$  through  $\pi$ - $\pi$  interactions. We experimentally demonstrated a high  $S^2\sigma$  derived from  $\pi$ - $\pi$  interactions and thoroughly investigated the  $S^2\sigma$  enhancement mechanism. This study would contribute to the development of thermoelectric performance enhancement in graphene-based materials.

## 2. Experimental

Graphene/PEDOT:PSS thin films  $(GP_n)$  were fabricated by spincoating graphene ink (n layers), followed by PEDOT:PSS ink, as shown in Fig. 1(a). The details of spin-coating are shown below. Graphene ink (900960, Sigma-Aldrich) and PEDOT:PSS ink (102671187, Sigma-Aldrich) were first sonicated using a sonication machine (AS ONE Ultrasonic Cleaner). In addition, 10 × 10 mm glass substrates (DAICO MFG Co., Ltd, Labo-USQ) were cleaned for 15 minutes using a UV ozone cleaner (UV253 MINI, Filgen, Inc.). Then, 33 μL of graphene ink was dropped onto a glass substrate set on a spin coater (MIKASA, MS-B100) and spin-coated at 2000 rpm for 30 seconds. This operation was performed n (=1, 2, 3, and 4) times. 100  $\mu$ L of PEDOT:PSS was dropped onto it and spin-coated at 2000 rpm for 30 seconds. These processes of spin coating of graphene and PEDOT:PSS were repeated. Finally, the thin films were annealed on a hot

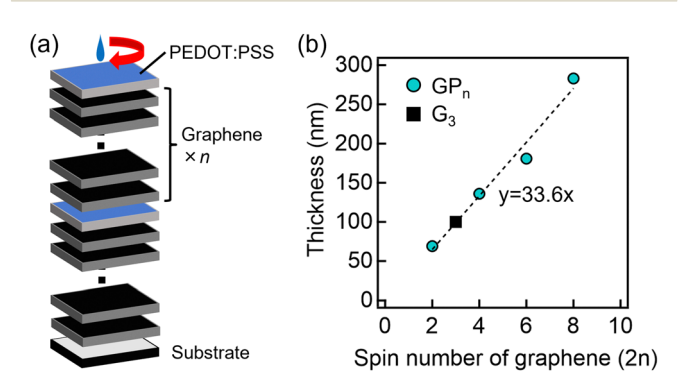


Fig. 1 (a) Schematic diagram of the fabrication process of  $GP_n$  and (b) the relationship between the number of graphene spin coating cycles (2n) and film thickness. In (b), the dashed line is a linear approximation line.

plate (AS ONE, CHPS-170DF) at 300 °C for 20 minutes in air. Graphene and PEDOT:PSS single-phase thin films were also prepared under similar conditions by spin-coating three times, which are denoted as G<sub>3</sub> and P<sub>3</sub>.

The structures of these thin films were evaluated by X-ray diffraction (XRD) using an X-ray diffractometer (Rigaku, SmartLab), scanning electron microscopy (SEM)-energy dispersive X-ray spectroscopy (EDX) using a field emission SEM (Hitachi High-Technologies, S-5500), atomic force microscopy (AFM; Agilent Technologies), and Raman spectroscopy (Lambda Vision, Micro-RAM300/CHK-532-785-Gr1). For Raman spectroscopy, a 532 nm (30 mW) light source and a 50× objective lens were used. The electronic states were evaluated by X-ray photoelectron spectroscopy (XPS) with the characteristic X-ray source of Al Kα radiation (IEOL, IPS-9010).

 $\sigma$  was calculated from the sheet resistance measured by the van der Pauw method and film thickness measured using the cross-sectional SEM images of cut samples.  $S = (-\Delta V/\Delta T)$  was calculated from the voltage difference  $(\Delta V)$  and temperature difference  $(\Delta T)$  measured with a self-made system and corrected with ZEM-3 (ADVANCE RIKO). Carrier concentration and mobility were measured by Hall effect measurements. Local electrical conductivity was measured by a 4-probe method with a probe distance of 100 μm.

### Results and discussion

A cross-sectional SEM image of the GP3 sample is shown in Fig. S1 (ESI†). The upper and lower sides of the boundary indicated by the arrows are different from each other. The lower side is the glass substrate and the upper side is the thin film. The thickness of this thin film was approximately 180 nm. By plotting the film thickness of the prepared samples against the number of graphene spin-coating cycles (Fig. 1(b)), we found that the plots can be approximated by a straight line through the origin. The results indicate that almost the same amount of graphene is formed in each spin coating.

The inset of Fig. 2(a) shows a photograph of the thin film surface in the GP<sub>3</sub> sample, showing an agglomerated PEDOT: PSS area and an exposed graphene region on the thin film. The area around the agglomerated PEDOT:PSS was observed by surface SEM (Fig. 2(a)), showing that the agglomerated PEDOT: PSS area was less uneven, while the exposed graphene region was more uneven. Elemental mapping by SEM-EDX revealed that the agglomerated PEDOT:PSS contained a large amount of S (Fig. 2(b)), which is attributed to PEDOT:PSS. From the above results, PEDOT:PSS agglomerated on graphene layers.

The structures of the agglomerated PEDOT:PSS region and the exposed graphene region mentioned above were analyzed in more detail. Fig. 2(c) and (d) show the Raman spectra of the PEDOT:PSS and graphene regions of the GP<sub>3</sub> sample, respectively. In the PEDOT:PSS region of the GP<sub>3</sub> sample (Fig. 2(c)), a typical Raman band at 1449 cm<sup>-1</sup> corresponding to the C=C symmetric stretching vibration of PEDOT was observed, where the peak position shifted to the higher wavenumber side

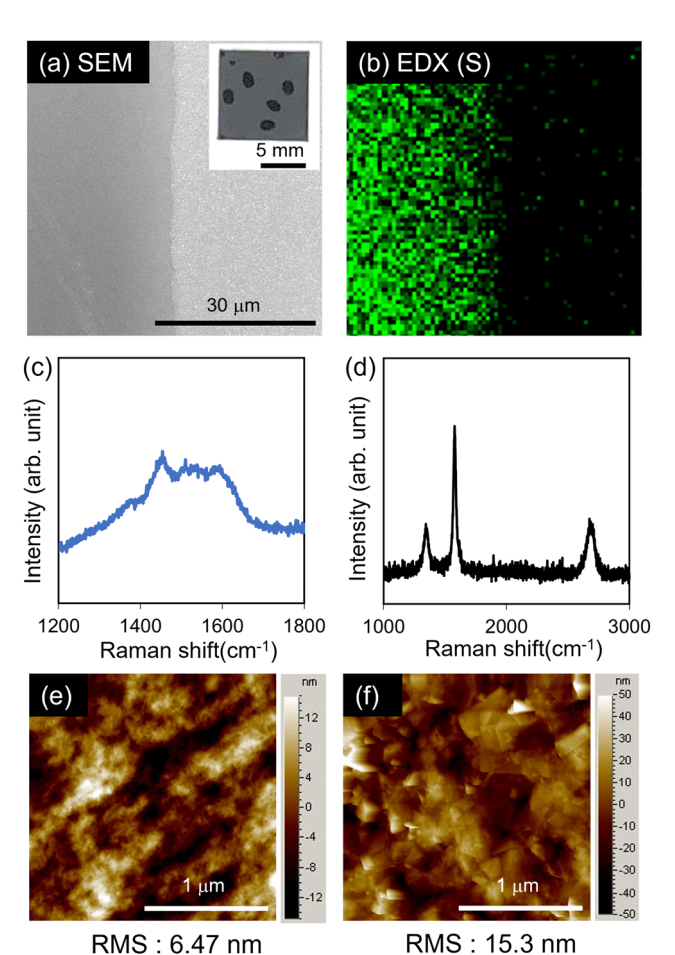


Fig. 2 (a) SEM image and (b) EDX elemental mapping image (S) of the  $GP_3$  sample surface. The inset in (a) shows the surface image. Raman spectra of (c) PEDOT:PSS and (d) graphene region of the  $GP_3$  sample. AFM images of (e) PEDOT:PSS and (f) graphene region of the  $GP_3$  sample.

compared to the peak position of  $1447 \text{ cm}^{-1}$  in  $P_3$  (Fig. S2, ESI†). This is due to the  $\pi$ - $\pi$  interaction between graphene and PEDOT. This is due to the  $\pi$ - $\pi$  interaction between graphene and PEDOT. Raman bands were also observed around 1520 cm<sup>-1</sup> and 1600 cm<sup>-1</sup> originating from the C=C asymmetric and antisymmetric stretching vibrations of PEDOT, The respectively, which are also observed in  $P_3$ . On the other hand, in the graphene region (Fig. 2(d)), three typical Raman bands were observed: a G band at approximately 1578 cm<sup>-1</sup> originating from the in-plane vibrational motion of sp² hybridized carbon, and D and 2D bands at around 1346 cm<sup>-1</sup> and 2683 cm<sup>-1</sup>, respectively, associated with overtones from the stretching motion of sp³ hybridized carbon. These Raman bands were also observed at similar wavenumbers in  $G_3$  (Fig. S2, ESI†).

Fig. 2(e) and (f) show the AFM images of the PEDOT:PSS and graphene regions of the  $GP_3$  sample, respectively. The PEDOT:PSS region of the  $GP_3$  sample shows fibrous morphology, while  $P_3$  exhibits a random granular structure (Fig. S2, ESI†). This is because PEDOT:PSS typically has a coiled structure and random molecular arrangement, whereas due to the  $\pi$ - $\pi$  interaction with graphene, PEDOT grows along the surface of graphene nanosheets, transforming the coiled structure into

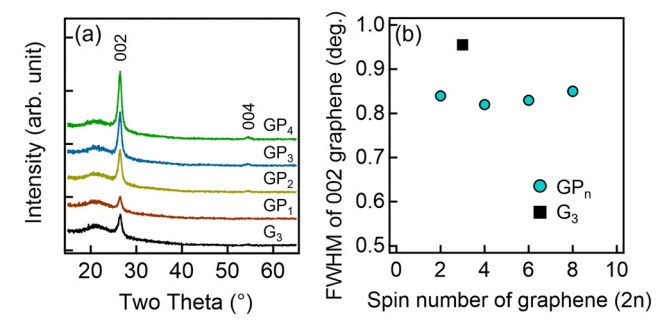


Fig. 3 (a) XRD  $2\theta-\omega$  scans for each thin film and (b) the dependence of the FWHM of the 002 graphene peak on the number of graphene spin coating cycles (2*n*).

a linear one and its random molecular arrangement into an ordered arrangement. <sup>46</sup> In the AFM images of both  $G_3$  and the graphene region of the  $GP_3$  sample, multiple sheet structures were observed. <sup>47</sup> The RMS roughness of the graphene region of the  $GP_3$  sample was approximately 15 nm, which is comparable to that of  $G_3$  ( $\sim$  20 nm).

Fig. 3(a) shows the XRD  $2\theta$ - $\omega$  scans of the GP<sub>n</sub> and G<sub>3</sub> samples. For all samples, the glass substrate-derived peak at 21.7° and the 002 and 004 diffraction peaks of graphene at 26.4° and 54.5°, respectively, were observed. As shown in Fig. 3(a), the 002 diffraction peak intensity increased with the number of graphene spin-coating cycles. The plot of the 002 diffraction peak intensity, normalized by the glass substrate peak, against the number of graphene spin-coating cycles was approximated with a straight line through the origin (Fig. S3, ESI†). This indicates that the amount of graphene in the thin films increased proportionally with the number of spin coating cycles, which is consistent with the results shown in Fig. 1(b). Fig. 3(b) shows the full width at half maximum (FWHM) of the 002 diffraction peak of graphene. All  $GP_n$  samples exhibited a reduced FWHM compared to G3. This suggests a smaller variation in the interlayer spacing of graphene, leading to high crystallinity, likely due to  $\pi$ - $\pi$  interactions with PEDOT.<sup>44</sup>

Fig. 4 shows the S (2p) XPS spectra of the PEDOT:PSS region in  $GP_3$  and  $P_3$  samples. Two peaks were observed at 166–170 eV and 162–166 eV attributed to sulfur in PSS and PEDOT, respectively. Notably, the PSS-derived peak intensity was lower for the

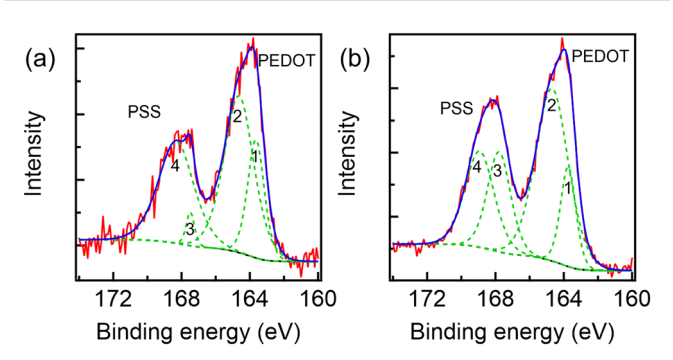


Fig. 4  $\,$  S (2p) XPS spectra of (a) GP $_3$  and (b) P $_3$  samples. The blue lines represent the sum of curves fitted with four components (dashed curves).

Table 1 Fitting results of S (2p) XPS spectra

Paper

Sample	Component	Center (eV)	Area ratio (%)	
GP <sub>3</sub>	1	163.6	18.8	
	2	164.6	44.4	
	3	167.5	2.6	
	4	168.3	34.2	
$P_3$	1	163.7	12.4	
	2	164.7	46.0	
	3	167.8	18.9	
	4	168.9	22.7	

GP<sub>3</sub> sample compared to P<sub>3</sub>, indicating a reduction in the amount of PSS present at or near the surface detectable by XPS. This reduction can be caused by a reorganization within the PEDOT:PSS complex facilitated by the  $\pi$ - $\pi$  interactions between graphene and PEDOT. The PEDOT-derived peak (162-166 eV) was fitted with two mixed Gaussian/Lorentzian functions, revealing peaks centered at 163.6 eV (neutral PEDOT) and 164.6 eV (oxidized PEDOT). 48 These fitting results are summarized in Table 1. The GP<sub>3</sub> sample exhibited a higher ratio of the neutral PEDOT component compared to P3, potentially due to the electron transfer from graphene to PEDOT:PSS. Furthermore, the PEDOT-derived peaks showed a slight shift towards lower binding energies in the GP<sub>3</sub> sample, indicating the reduction of PEDOT, which is consistent with previous reports. 49 Additionally, the peak corresponding to sulfur atoms in ionic PSS (component 3) decreased for the GP3 sample compared with P3. This is likely because PSS interacts less strongly with the PEDOT chains due to stronger PEDOTgraphene interactions.

The S,  $\sigma$  and  $S^2\sigma$  values of the fabricated thin films plotted against the number of graphene spin-coating cycles are shown in Fig. 5(a)-(c), respectively. Fig. 5(a) shows that the  $GP_n$ samples exhibited S values similar to those of graphene, except

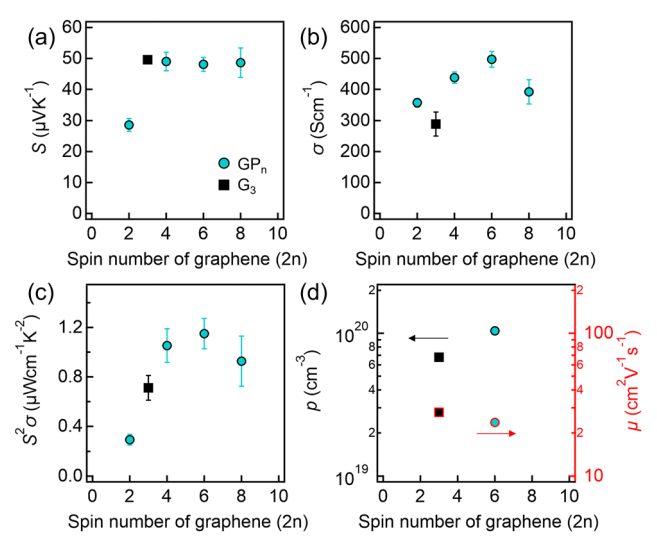


Fig. 5 The dependences of (a) S, (b)  $\sigma$ , (c)  $S^2\sigma$ , and (d) p (left axis) and  $\mu$ (right axis) on the number of graphene spin coating cycles (2n) for each thin film.

for  $GP_1$ . In contrast, the  $\sigma$  values of the  $GP_n$  samples were higher than those of  $G_3$ . Notably, the  $GP_3$  sample exhibited a  $\sigma$ value approximately 1.7 times higher than that of G<sub>3</sub>. Additionally,  $GP_n$  samples also exhibited higher S and  $\sigma$  than those of the PEDOT:PSS single-phase thin film ( $S \approx 4 \mu V K^{-1}, \sigma \approx$ 46 S cm<sup>-1</sup>). Consequently, the  $S^2\sigma$  value increased by about 1.6 times compared with G<sub>3</sub>, as shown in Fig. 5(c). To investigate the origin of this high  $S^2\sigma$ , carrier concentration (p) and Hall mobility  $(\mu)$  were measured by Hall effect measurements. As shown in Fig. 5(d), the  $GP_3$  sample exhibited higher p in contrast to its lower Hall mobility when compared to  $G_3$ . This observation can be attributed to the electron transfer from graphene to PEDOT within the GP<sub>3</sub> sample. This electron transfer is facilitated by the strong  $\pi$ - $\pi$  interactions between the graphene and the conjugated polymer of PEDOT. 36,39 However, a drop in  $\sigma$  was observed for the GP<sub>4</sub> sample as shown in Fig. 5(b), which is due to a reduced effective interaction ratio between the PEDOT:PSS and the graphene layers with the increase of the number of graphene layers.

To investigate the carrier transport in detail, we measured the temperature dependence of the electrical properties of GP<sub>3</sub> and  $G_3$ . As shown in Fig. 6(a), the  $\sigma$  of both samples slightly increased as the temperature increased, indicating their semiconductor-like properties. In some previous reports, the carrier transport mechanism in reduced graphene oxide has been discussed using the Mott-variable range hopping (VRH) model and thermal activation.<sup>50</sup> In the case of the threedimensional Mott-VRH model,  $\sigma$  exhibits a T dependence given by  $\sigma \propto \exp(-(T_0/T)^{-1/4})$ , where  $T_0$  is the Mott characteristic temperature. However, the VRH model does not provide a good fit to the  $\sigma$  of GP<sub>3</sub> and G<sub>3</sub> because our samples show a

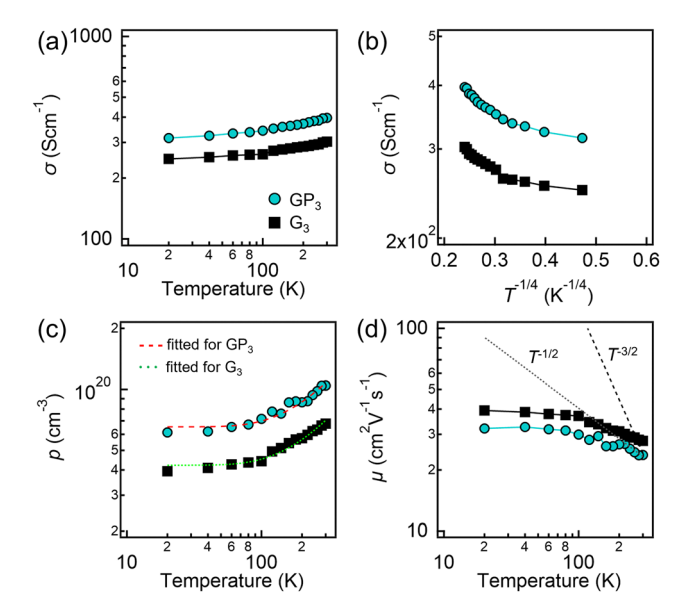


Fig. 6 Temperature dependences of the electrical properties of GP<sub>3</sub> and G<sub>3</sub> samples: (a)  $\sigma$  vs. T, (b)  $\sigma$  vs.  $T^{-1/4}$ , (c) p vs. T, and (d)  $\mu$  vs. T. In (c), the dashed and dotted lines represent the fitting curves for  $GP_3$  and  $G_3$ samples, respectively. In (d), the dashed and dotted lines represent the temperature dependence of  $\mu \propto T^{-3/2}$  and  $\mu \propto T^{-1/2}$ , respectively.

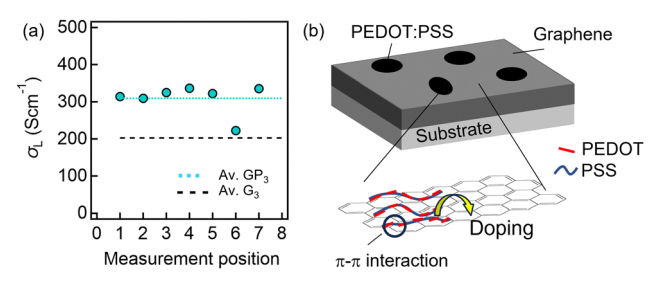


Fig. 7 (a) Local electrical conductivity ( $\sigma_{\rm L}$ ) in various graphene regions in GP<sub>3</sub> and (b) schematic diagram of graphene doping from PEDOT:PSS *via* local  $\pi-\pi$  interactions.

nonlinear  $T^{-1/4}$  dependence of the logarithm of  $\sigma$ , as shown in Fig. 6(b).

Fig. 6(c) shows the T dependence of p. The p was fitted with the following equation based on a simple two-band model of bulk graphite:<sup>35,51</sup>

$$p = p_{g} + p_{d}$$

$$= C_{g}k_{B}T \ln \left[ 1 + \exp\left(\frac{\delta E_{g}}{2k_{B}T}\right) \right]$$

$$+ C_{d}k_{B}T \ln \left[ 1 + \exp\left(\frac{\delta E_{d}}{2k_{B}T}\right) \right],$$
(1)

where  $p_g$  and  $p_d$  are the carrier concentrations of  $G_3$  and the contribution of doped graphene from PEDOT:PSS.  $C_g$  and  $C_d$  are constants,  $k_B$  is the Boltzmann constant, and  $\delta E_g$  and  $\delta E_d$  are the band overlap (shown in the inset of Fig. 6(c)). The dashed and dotted lines in Fig. 6(c) represent the fitting curves for  $GP_3$  and  $G_3$ , respectively. These curves are in good agreement with the experimental data. In the case of  $G_3$ , the experimental data were fitted with  $C_d = 0$ . The  $\delta E_g$  was obtained as  $33 \pm 2$  meV. In contrast, the p of  $GP_3$  was fitted with fixed values of  $C_g$  and  $\delta E_g$  as mentioned above. The  $\delta E_d$  was obtained as  $35 \pm 5$  meV, which is similar to  $\delta E_g$ . This result revealed that the  $GP_3$  sample achieved high carrier concentration through doping from PEDOT. Because PEDOT:PSS agglomerated on graphene layers, the high carrier concentration is mainly due to the contribution of graphene layers.

The Hall mobilities of  $GP_3$  and  $G_3$  as a function of T are shown in Fig. 6(d). The  $\mu$  values of both  $GP_3$  and  $G_3$  decreased as T increased. Considering that the dependence is similar for both samples,  $GP_3$  likely exhibits similar carrier scattering mechanisms to  $G_3$ . This decrease in dependence might be considered to arise from acoustic phonon scattering. Although, in general, the large contribution of acoustic phonon scattering tends to be proportional to  $T^{-3/2}$  (dashed line), the experimental value exhibits a weaker dependence than  $T^{-1/2}$  (dotted line). Therefore, the carrier scattering mechanism must be extremely complicated because it might contain some other carrier scattering processes such as those caused by impurities, defects, interfaces, etc. Based on the above discussion, the high  $S^2\sigma$  of  $GP_3$  originating from high  $\sigma$  is attributed to the enhancement of p by doping from PEDOT due to the  $\pi$ - $\pi$  interactions.

**Table 2** Comparison of the thermoelectric properties ( $\sigma$ , S, and  $S^2\sigma$ ) of graphene–PEDOT:PSS samples in previous studies and this work (GP<sub>3</sub>)

Sample	$\sigma$ (S cm <sup>-1</sup> )	$S (\mu V K^{-1})$	$S^2 \sigma$ ( $\mu W \text{ cm}^{-1} \text{ K}^{-2}$ )	Ref.
This work	497	48	1.2	_
Graphene	81	41	0.187	35
PEDOT:PSS/graphene (70 wt%)	96	17	0.029	41
PEDOT:PSS/graphene (RTCVD)	193	54	0.054	42
PEDOT:PSS/rGO (2 wt%)	32	59	0.11	38
PEDOT:PSS/rGO (3 wt%)	637	27	0.46	37
PEDOT:PSS/rGO (16 wt%)	51	61	0.050	36
PEDOT:PSS/rGO (20 wt%)	410	61	1.5	40
PEDOT:PSS/GQD (13 wt%)	72	15	0.015	39

Despite the agglomeration of PEDOT:PSS on graphene, the abovementioned thermoelectric properties were measured over the entire region. To understand the relationship between the electrical properties and the local structures, it is essential to measure local electrical properties. Here, the local electrical conductivity  $(\sigma_L)$  of the  $GP_3$  sample was measured using a 4-probe method. Fig. 7(a) shows the  $\sigma_L$  at various positions in the graphene region of the GP3 sample; in the PEDOT:PSS region, the contact resistance was too high to measure  $\sigma_{\rm I}$ . Dotted and dashed lines indicate the average values of GP3 and  $G_3$ , respectively. The  $\sigma_L$  of the graphene region in the  $GP_3$ sample was obviously higher than that of G<sub>3</sub> in most areas. This indicates that the  $\sigma_L$  is high not only for graphene in contact with PEDOT:PSS, but also for the entire thin film, including the graphene region spatially distant from PEDOT:PSS. These results suggest that the local  $\pi$ - $\pi$  interactions with PEDOT:PSS contribute to the electron transfer from graphene to PEDOT and the enhanced crystallinity of graphene throughout the thin film, resulting in high  $S^2\sigma$  (Fig. 7(b)).

Finally, the  $S^2\sigma$  of the GP<sub>3</sub> sample fabricated in this study (1.2  $\mu$ W cm<sup>-1</sup> K<sup>2</sup>) was compared with those of previously reported PEDOT:PSS/graphene-based thin films (Table 2). The GP<sub>3</sub> sample prepared in this study exhibited high  $S^2\sigma$  comparable to a previous report (1.50  $\mu$ W cm<sup>-1</sup> K<sup>2</sup>) for PEDOT:PSS/rGO(20 wt%) prepared by the pad-dry-cure method. <sup>40</sup> In this study, through the formation of agglomerated PEDOT:PSS, a relatively high  $S^2\sigma$  was obtained despite the simplicity of the spin-coating method. Although the  $S^2\sigma$  values of GP<sub>n</sub> samples were relatively low compared with other inorganic thermoelectric materials, we believe that our fabrication approach can contribute to the development of graphene-based thermoelectric materials.

#### 4. Conclusions

In this study, we fabricated graphene/PEDOT:PSS thin films by a spin-coating method using graphene and PEDOT:PSS ink and evaluated their thermoelectric properties. In the thin films, PEDOT:PSS agglomerated on graphene thin films, which was observed by AFM and SEM-EDX. Raman spectroscopy and AFM analyses showed that the  $\pi$ - $\pi$  interactions between graphene and PEDOT transform the coil structure into a linear structure and the random molecular arrangement into an ordered one.

**Materials Advances Paper** 

The  $\pi$ - $\pi$  interactions stabilize the aromatic ring configuration and reduce variations in the graphene interlayer spacing. The  $S^2\sigma$  of 1.2  $\mu W$  cm<sup>-1</sup> K<sup>-2</sup> for the GP<sub>3</sub> sample is 1.6 times higher than that of  $G_3$ . The local  $\pi$ - $\pi$  interactions with PEDOT:PSS contribute to the electron transfer from graphene to PEDOT and the enhanced crystallinity of graphene throughout the thin film, resulting in high  $S^2\sigma$ .

#### **Author contributions**

K. U.: data curation, investigation, and writing - original draft; S. S.: conceptualization, methodology, formal analysis, funding acquisition, visualization, writing - original draft, writing review & editing; T. S.: investigation; A. A.: data curation; H. U.: writing - review & editing; H. T.: funding acquisition, supervision, writing - review & editing.

#### Conflicts of interest

There are no conflicts to declare.

## Data availability

The data supporting this article have been included as part of the ESI.†

## Acknowledgements

This work was supported by the Grant-in-Aid for Early-Career Scientists (Grant Number 21K14479) from JSPS KAKENHI Japan and JST-ALCA-Next Japan (Grant Number JPMJAN24B3). We thank the Open Facility Center for Research, Ibaraki University for technical assistance. We thank Prof. H. Chang and K. Katayama at Chuo University for their support with XRD and Raman spectroscopy, respectively.

#### References

- 1 J. Mao, H. Zhu, Z. Ding, Z. Liu, G. A. Gamage, G. Chen and Z. Ren, Science, 2019, 365, 495-498.
- 2 I. J. Yoo, Y. Song, D. C. Lim, N. V. Myung, K. H. Lee, M. Oh, D. Lee, Y. D. Kim, S. Kim, Y. H. Choa, J. Y. Lee, K. H. Leea and J. H. Lim, J. Mater. Chem. A, 2013, 1, 5430-5435.
- 3 F. Hao, P. Qiu, Y. Tang, S. Bai, T. Xing, H. S. Chu, Q. Zhang, P. Lu, T. Zhang, D. Ren, J. Chen, X. Shi and L. Chen, Energy Environ. Sci., 2016, 9, 3120-3127.
- 4 A. Ayukawa, N. Kiridoshi, W. Yamamoto, A. Yasuhara, H. Udono and S. Sakane, Appl. Phys. Express, 2024, 17,
- 5 Y. Lu, Y. Ding, Y. Qiu, K. Cai, Q. Yao, H. Song, L. Tong, J. He and L. Chen, ACS Appl. Mater. Interfaces, 2019, 11,
- 6 S. Sakane, T. Miura, K. Munakata, Y. Morikawa, S. Miwa, R. Yamanaka, T. Sugai, A. Ayukawa, H. Udono and H. Tanaka, Nanoscale Adv., 2024, 6, 3299-3305.

- 7 S. Sakane, S. Miwa, T. Miura, K. Munakata, T. Ishibe, Y. Nakamura and H. Tanaka, ACS Omega, 2022, 7, 32101-32107.
- 8 J. Zhang, L. Song, A. Mamakhel, M. R. V. Jørgensen and B. B. Iversen, Chem. Mater., 2017, 29, 5371-5383.
- 9 Y. Pan, M. Yao, X. Hong, Y. Zhu, F. Fan, K. Imasato, Y. He, C. Hess, J. Fink, J. Yang, B. Büchner, C. Fu, G. J. Snyder and C. Felsera, Energy Environ. Sci., 2020, 13, 1717.
- 10 X. Su, F. Fu, Y. Yan, G. Zheng, T. Liang, Q. Zhang, X. Cheng, D. Yang, H. Chi, X. Tang, Q. Zhang and C. Uher, Nat. Commun., 2014, 5, 4908.
- 11 Y. Ding, Y. Qiu, K. Cai, Q. Yao, S. Chen, L. Chen and J. He, Nat. Commun., 2019, 10, 841.
- 12 C. Xiao, J. Xu, K. Li, J. Feng, J. Yang and Y. Xie, J. Am. Chem. Soc., 2012, 134, 4287-4293.
- 13 W. Mi, P. Qiu, T. Zhang, Y. Lv, X. Shi and L. Chen, Appl. Phys. Lett., 2014, 104, 133903.
- 14 J. Tang, H. T. Wang, D. H. Lee, M. Fardy, Z. Huo, T. P. Russell and P. Yang, Nano Lett., 2010, 10, 4279-4283.
- 15 J. Tani and H. Kido, *Physica B*, 2005, **364**, 218–224.
- 16 S. Sakane, T. Ishibe, T. Taniguchi, T. Hinakawa, R. Hosoda, K. Mizuta, M. M. Alam, K. Sawano and Y. Nakamura, *Jpn.* J. Appl. Phys., 2020, 59, SFFB01.
- 17 S. Sakane, T. Ishibe, T. Taniguchi, N. Naruse, Y. Mera, T. Fujita, M. M. Alam, K. Sawano, N. Mori and Y. Nakamura, Mater. Today Energy, 2019, 13, 56-63.
- 18 J. L. Blackburn, A. J. Ferguson, C. Cho and J. C. Grunlan, Adv. Mater., 2018, 30, 1704386.
- 19 O. Y. Li, T. Feng, W. Okita, Y. Komori, H. Suzuki, T. Kato, T. Kaneko, T. Ikuta, X. Ruan and K. Takahashi, ACS Nano, 2019, 13, 9182-9189.
- 20 S. Sakane, T. Ishibe, Y. Yukawa and Y. Nakamura, Diamond Relat. Mater., 2023, 140, 110410.
- 21 X. Wang, H. Wang and B. Liu, Polymers, 2018, 10, 1196.
- 22 Y. Xu, Z. Li and W. Duan, Small, 2014, 10(11), 2182-2199.
- 23 M. Sang, J. Shin, K. Kim and K. J. Yu, Nanomaterials, 2019, 9, 374.
- 24 P. Dollfus, V. H. Nguyen and J. Saint-Martin, J. Phys.: Condens. Matter, 2015, 27, 133204.
- 25 A. Sharma, S. Sharma and S. Ajori, J. Mater. Sci., 2023, 58, 10222-10260.
- 26 A. H. C. Neto, F. Guinea, N. M. R. Peres, K. S. Novoselov and A. K. Geim, Rev. Mod. Phys., 2009, 81, 1.
- 27 S. D. Sarma, S. Adam, E. H. Hwang and E. Rossi, Rev. Mod. Phys., 2011, 83, 2.
- 28 K. S. Novoselov, A. K. Geim, S. V. Morozov, D. Jiang, Y. Zhang, S. V. Dubonos, I. V. Grigorieva and A. A. Firsov, Science, 2004, 306, 666-669.
- 29 A. H. Reshak, S. A. Khan and S. Auluck, J. Mater. Chem. C, 2014, 2, 2346-2352.
- 30 H. J. Goldsmid and J. W. Sharp, J. Electron. Mater., 1999, 28, 7.
- 31 J. Duan, X. Wang, X. Lai, G. Li, K. Watanabe, T. Taniguchi, M. Zebarjadi and E. Y. Andrei, Proc. Natl. Acad. Sci. U. S. A., 2016, 113, 14272-14276.
- 32 Y. M. Zuev, W. Chang and P. Kim, Phys. Rev. Lett., 2009, 102, 96807.

- 33 S. G. Nam, D. K. Ki and H. J. Lee, *Phys. Rev. B: Condens. Matter Mater. Phys.*, 2010, **82**, 245416.
- 34 K. Kanahashi, M. Ishihara, M. Hasegawa, H. Ohta and T. Takenobu, *npj 2D Mater. Appl.*, 2019, 3, 44.
- 35 T. Juntunen, H. Jussila, M. Ruoho, S. Liu, G. Hu, T. Albrow-Owen, L. W. T. Ng, R. C. T. Howe, T. Hasan, Z. Sun and I. Tittonen, *Adv. Funct. Mater.*, 2018, **28**, 1800480.
- 36 K. Xu, G. Chen and D. Qiu, *J. Mater. Chem. A*, 2013, 1, 12395–12399.
- 37 D. Yoo, J. Kim and J. H. Kim, Nano Res., 2014, 7(5), 717-730.
- 38 G. H. Kim, D. H. Hwang and S. I. Woo, *Phys. Chem. Chem. Phys.*, 2012, **14**, 3530–3536.
- 39 F. P. Du, N. N. Cao, Y. F. Zhang, P. Fu, Y. G. Wu, Z. D. Lin, R. Shi, A. Amini and C. Cheng, Sci. Rep., 2018, 8, 6441.
- 40 N. A. Khoso, X. Jiao, X. G. Yu, S. Tian and J. Wang, RSC Adv., 2021, 11, 16675.
- 41 J. Liu, G. Liu, J. Xu, C. Liu, W. Zhou, P. Liu, G. Nie, X. Duan and F. Jiang, *ACS Appl. Energy Mater.*, 2020, 3, 6165–6171.
- 42 C. Park, D. Yoo, J. J. Lee, H. H. Choi and J. H. Kim, *Org. Electron.*, 2016, **36**, 166–170.
- 43 Y. Chen, J. Xu, Y. Yang, S. Li, W. Yang, T. Peng, X. L. Mao and Y. Zhao, *J. Mater. Sci: Mater. Electron.*, 2015, **26**, 8292–8300.

- 44 Y. Lu, Q. Yang, S. Wang, M. Liu, Y. Chen, Z. Zhao, A. R. Akbar, C. Xiong and G. H. Hu, *Ionics*, 2021, 27, 3615–3626.
- 45 N. Soin, S. S. Roy, C. O'Kane, J. A. D. McLaughlin, T. H. Limb and C. J. D. Hetherington, *CrystEngComm*, 2011, 13, 312–318.
- 46 V. C. Tung, J. Kim, L. J. Cote and J. Huang, J. Am. Chem. Soc., 2011, 133, 9262–9265.
- 47 Z. M. Marković, M. D. Budimir, D. P. Kepić, I. D. Holclajtner-Antunović, M. T. Marinović-Cincović, M. D. Dramićanin, V. D. Spasojević, D. B. Peruško, Z. Špitalský, M. Mičušik, V. B. Pavlović and B. M. Todorović-Marković, *RSC Adv.*, 2016, 6, 39275–39283.
- 48 Y. Shirai, S. Takami, S. Lasmono, H. Iwai, T. Chikyow and Y. Wakayama, J. Polym. Sci., Part B: Polym. Phys., 2011, 49, 1762–1768.
- 49 J. H. Song, J. Jeong, J. Park, G. Park, I. Imae and J. Kwak, *ACS Appl. Electron. Mater.*, 2024, **6**, 6313–6321.
- 50 Y. Wang, Y. Chen, S. D. Lacey, L. Xu, H. Xie, T. Li, V. A. Danner and L. Hu, *Mater. Today*, 2018, **21**, 186–192.
- 51 K. Nagashio, T. Nishimura, K. Kita and A. Toriumi, *Jpn. J. Appl. Phys.*, 2010, **49**, 051304.